Journal of Structural Geology 161 (2022) 104672

Contents lists available at ScienceDirect

Journal of Structural Geology

journal homepage: www.elsevier.com/locate/jsg

Monazite as a monitor of shear strain in orogenic crust

Gregory Dumond [a,*], Kevin H. Mahan [b], Philippe Goncalves [c], Michael L. Williams [d], Michael J. Jercinovic [d]

[a] Department of Geosciences, University of Arkansas, Fayetteville, AR, 72701, USA
[b] Department of Geological Sciences, University of Colorado, Boulder, CO, 72701, USA
[c] Laboratoire Chrono-Environnement, Université de Bourgogne Franche-Comté, 25030, Besançon, France
[d] Department of Geosciences, University of Massachusetts, Amherst, MA, 01003, USA

ARTICLE INFO

Keywords:
Shear zone
Mylonite
Monazite
Continental crust
Dissolution precipitation creep
EBSD

ABSTRACT

The Ramsay-Graham heterogeneous simple shear zone model revolutionized our understanding of finite strain variation in orogenic belts. Many deeply exhumed (>20 km depths) shear zones in orogenic continental crust are a consequence of sub-simple shear strain accumulation during contraction and displacement at high temperature. Here we explore the micro-scale record of this process using syn-kinematic monazite in two shear zones in a >20,000 km^2 terrane of exhumed lower continental crust. Field observations combined with high-spatial resolution X-ray mapping, Th–U-Pb electron microprobe petrochronology, and electron backscatter diffraction analysis demonstrate that monazite grains can provide an important textural and temporal record of shear strain in mylonite and ultramylonite gneisses. Monazite grains exhibit aspect ratios of 1.7–4.6 parallel to the stretching lineation and parallel or oblique (<30°) to the penetrative foliation. Monazite EBSD data for grain orientation spread, i.e., average misorientation relative to the mean, are consistent with no significant dislocation-accommodated internal deformation. We conclude that dissolution precipitation creep of monazite produced compositionally-defined geometries compatible with the dextral sense of shear observed in outcrop and thin section. Syn-kinematic rims on monazite grains that develop in low strain domains during accumulation of shear strain can provide absolute ages for μm-to km-scale kinematics in continental orogens.

1. Introduction

Strain localization and ductile deformation in middle to lower continental crust during orogeny commonly involves mm-to km-scale shear zones (Ramsay, 1980; Bürgmann and Dresen, 2008; Fossen and Cavalcante, 2017; Ceccato et al., 2020). In orogens, shear zone development and propagation are critical for accommodating plate-scale deformation in orogenic wedges (Thigpen et al., 2013; Jabaloy-Sánchez et al., 2015), orogenic channels (Grujic et al., 2002; Jannin et al., 2018), orogenic plateaus (Andronicos et al., 2007; Bajolet et al., 2015), and magmatic arcs (Tikoff and de Saint Blanquat, 1997; Andronicos et al., 1999). The exhumed record of shear zone development and evolution in these settings can be difficult to date, particularly when strain accumulation was episodic as a result of reactivation (Shaw et al., 2001; Dumond et al., 2008).

The age of displacement along ductile shear zones is commonly determined by bracketing the dates between which displacement occurred using variably deformed dikes and/or sills (Cottle et al., 2015). A disadvantage of this approach is that the age of displacement is not uniquely determined. One approach for overcoming this problem is to identify dikes that were emplaced synchronous with respect to displacement (Sassier et al., 2009). Syn-kinematic emplacement of dikes during shearing, however, can be difficult to unequivocally demonstrate. An alternative approach involves identifying syn-kinematic geochronometers *in situ* that crystallized or recrystallized simultaneously with shear strain accumulation, e.g., muscovite at $T = 300$–425 °C (Cliff and Meffan-Main, 2003; Hueck et al., 2020; Beaudoin et al., 2021; Lin et al., 2021) titanite at $T = 650$->800 °C (Storey et al., 2004; Gordon et al., 2021), and monazite at $T = 530$->800 °C (Mahan et al., 2006; Dumond et al., 2008; Langille et al., 2012; Dumond, 2020). For *in situ* dating of high temperature ductile shear zone development, monazite is more advantageous due to its widespread occurrence in metapelites and metagreywackes (Warren et al., 2018), leucogranites (Dumond et al., 2008; Lederer et al., 2013), and felsic granulites (Mahan et al., 2006;

* Corresponding author.
E-mail address: gdumond@uark.edu (G. Dumond).

https://doi.org/10.1016/j.jsg.2022.104672
Received 22 October 2021; Received in revised form 14 June 2022; Accepted 28 June 2022
Available online 6 July 2022

Dumond et al., 2015, 2017). Over the last two decades, there is increasing recognition of monazite-bearing shear zones in a variety of tectonic settings that span the Archean to the Miocene: Archean sub-horizontal lower crustal flow in the Canadian Shield (Dumond et al., 2010), Paleoproterozoic crustal-scale thrust shear zone systems that uplift lower crust (Mahan et al., 2006), Mesoproterozoic intra-continental shear zones in the American Southwest (Shaw et al., 2001), and Oligocene-Miocene detachment zones associated with Himalayan gneiss domes (Langille et al., 2012).

The Th- and LREE-rich (light rare earth element: La to Gd) phosphate

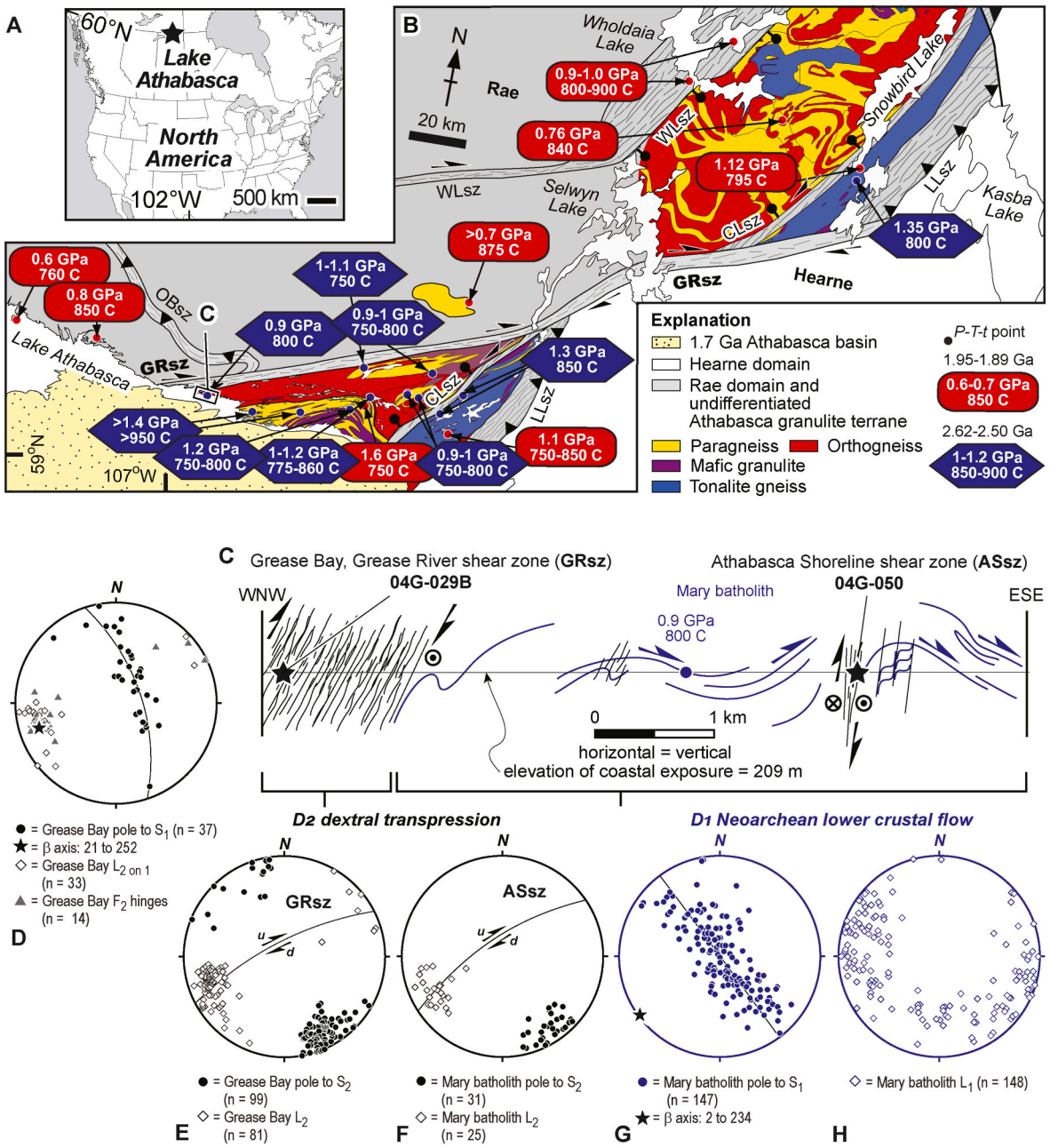

Fig. 1. **A)** Location (black star) of Athabasca granulite terrane in western Canadian Shield of North America. **B)** Geologic map of the Athabasca granulite terrane modified from Dumond et al. (2018). Note rectangular box indicating the location of the mapped region in Fig. 1C. Abbreviations are: WLsz = Wholdaia Lake shear zone (Thiessen et al., 2018); CLsz = Cora Lake shear zone (Regan et al., 2014); LLsz = Legs Lake shear zone (Mahan et al., 2003, 2006); GRsz = Grease River shear zone (Dumond et al., 2008; Dumond, 2020); OBsz = Oldman-Bulyea shear zone (Card, 2001; Dumond et al., 2013). Note locations of Pressure-Temperature-time (*P-T*-t) data. Blue *P-T* points represent regions of Neoarchean high pressure metamorphism and melting that subsequently experienced protracted isobaric cooling. Red *P-T* points are high temperature domains that experienced partial melting ± decompression in the Paleoproterozoic. **C)** Geologic cross-section along the north shore of Lake Athabasca encompassing the eastern margin of the Grease River shear zone at Grease Bay and the Athabasca Shoreline shear zone (modified from Dumond et al., 2010). **D)** Stereonet of Paleoproterozoic S_1 foliations preserved in low strain domains of the GRsz, associated with gently SW-plunging minor folds and intersection lineations. **E)** Stereonet for the dextral NE-striking transpressive GRsz with predominantly gently SW-plunging L_2 stretching lineations. **F)** Stereonet for dextral NE-striking transpressive shear zones with gently SW-plunging L_2 stretching lineations in the Mary batholith, including the Athabasca Shoreline shear zone (ASsz). **G)** Stereonet of poles to Neoarchean S_1 gneissic foliations in the Mary batholith with β-axis depicting near horizontal F_2 folds. **H)** Stereonet of folded Neoarchean L_1 stretching lineations in the Mary batholith. (For interpretation of the references to color in this figure legend, the reader is referred to the Web version of this article.)

mineral monazite has been used to date several fundamental tectonic processes in continental crust (Williams et al., 1999; Krohe and Wawrzenitz, 2000; Williams and Jercinovic, 2002, 2012; Wawrzenitz et al., 2012). These processes include faulting (Bergemann et al., 2018), shear zone development (Shaw et al., 2001; Mahan et al., 2006; Dumond et al., 2008; Regan et al., 2014), melting (Pyle and Spear, 2003; Yakymchuk and Brown, 2014; Dumond et al., 2015), lower crustal flow (Dumond et al., 2010), pluton emplacement (Cottle et al., 2019), formation of veins, clefts, and fissures (Berger et al., 2013; Fitz-Diaz et al., 2019; Gnos et al., 2021), and the formation of large U deposits (Jeanneret et al., 2017). The success of monazite for constraining these processes is largely due to: (i) its susceptibility to fluid-mediated dissolution-reprecipitation and crystal plastic deformation (Seydoux-Guillaume et al., 2002; Hetherington et al., 2010; Harlov et al., 2011; Williams et al., 2011; Wawrzenitz et al., 2012, 2015; Erickson et al., 2015, 2016; Wawrzenitz and Krohe, 2016), and (ii) advances in high-spatial resolution *in situ* microanalysis via electron microprobe (Jercinovic et al., 2008; Williams et al., 2017; Allaz et al., 2019), laser ablation inductively coupled plasma mass spectrometry (Paquette and Tiepolo, 2007; Kylander-Clark et al., 2013), and ion probe (Fletcher et al., 2010; Berger et al., 2013).

We combine published and new data on monazite grains in two lower crustal dextral transpressive shear zones to highlight the utility of syn-kinematic monazite for constraining micro-to orogen-scale kinematics and episodic shear strain accumulation. These data come from the deeply exhumed 2.61–1.80 Ga Athabasca granulite terrane, Saskatchewan and Northwest Territories, Canada (>0.6–1.6 GPa; Fig. 1; Dumond et al., 2018). Previously unreported field observations are combined with new high-spatial resolution X-ray mapping, electron backscatter diffraction analysis, and Th–U-Pb electron microprobe petrochronology to demonstrate that monazite grains provide a key textural and temporal record of shear strain in mylonite and ultramylonite gneisses. We suggest the occurrence of syn-kinematic monazite domains in granite, metapelite, metagreywacke, and felsic granulite tectonites in high strain zones provides an important tool for constraining the timing, duration, and variation of strain in shear belts such as those explored and first quantified by Ramsay and Graham (1970).

2. Methods

2.1. High-spatial resolution X-ray mapping, optical microscopy, and kinematic analysis

Oriented hand samples were collected from each outcrop, and thin sections were cut from each sample parallel to the outcrop-scale stretching lineation and perpendicular to the penetrative gneissic foliation to yield sections inferred to represent the XZ-plane of finite strain. Monazite grains in polished thin sections were identified via high-spatial resolution X-ray mapping. Full section X-ray stage maps were obtained using the Cameca SX50 and SX 100 electron microprobes at the Electron Microprobe/SEM Facility at the University of Massachusetts-Amherst. Stage maps were run at 15 kV and 300 nA using a 35 μm beam, 35 μm step size, and 25–80 ms dwell time. X-ray beam raster maps for Y *L*α, Ca *K*α, Th *M*α, and U *M*β were generated for each monazite grain at 15 kV and 200 nA using a focused beam, 0.3–0.5 μm step size, and a 50–100 ms dwell time (see Williams et al., 2017). Optical microscopy and vorticity analysis were carried out using a Leica DM2500P polarization and reflected light microscope connected to a Leica DMC 5400 20.0 megapixel digital camera. Thin sections were aligned with respect to the foliation to measure the aspect ratio of each monazite grain and the angle between the long axis of each grain and the foliation using the Leica Application Suite X Measurements Module. Kinematic analysis in thin section was supplemented by outcrop analysis of strain markers, e.g., mantled porphyroclasts and oblique grain shapes.

2.2. Th–U-Pb electron probe microanalysis (EPMA) and petrochronology

Monazite major and trace element analysis for Th–U-Pb dating was done using the Cameca Ultrachron SX-100 electron microprobe with a LaB_6- or CeB_6-source in the Electron Microprobe/SEM Facility at the University of Massachusetts-Amherst, following the approach of Jercinovic et al. (2008) and Williams et al. (2017). A description of major and trace element standards is presented in Dumond et al. (2008). Background corrections for Th–U–Pb and trace elements was done using the multi-point background approach of Allaz et al. (2019). Analyses were carried out using a focused beam at 15 kV and 200 nA. Monazite Th–U-Pb dates and 2σ errors were calculated according to Williams et al. (2006). Calibrations were periodically checked throughout each analytical session by analyzing a consistency standard (Williams et al., 2006). The standard used in this study is the Moacir Brazilian pegmatite monazite with a weighted mean $^{207}Pb/^{235}U$ age of 504.3 ± 0.2 Ma (2σ, MSWD = 0.64; Gasquet et al., 2010).

2.3. Electron backscatter diffraction (EBSD) analysis

EBSD data were collected at the Colorado Shared Instrumentation in Nanofabrication and Characterization (COSINC) facility at the University of Colorado-Boulder. Analysis was carried out using a W-source Hitachi SU3500 SEM under low vacuum conditions (10 Pa) and using a 15 kV accelerating voltage with a ~7 nA sample current. The SEM is equipped with an Oxford Instruments Nordlys Nano EBSD camera with Aztec 4.2 software. We used the monazite match unit from Erickson et al. (2015), and other indexation parameters, including a Hough resolution of 70, 8 detected Kikuchi bands, and Oxford's Refined Accuracy indexing routine. All subsequent data processing was performed using the MTEX toolbox version 5.7 in MATLAB 2021a (Hielscher and Schaeben, 2008; Mainprice et al., 2014). A maximum mean angular deviation of detected Kikuchi bands from model bands (MAD) of 1° was used in all maps. Grain-detection utilized a 10° minimum misorientation threshold, and every grain was required to have a minimum of five indexed measurements (pixels), otherwise pixels were reassigned as non-indexed. During grain reconstruction in MTEX, we allow some regions of non-indexed data to remain non-indexed if the region had a ratio of total pixel area to continuous boundary length of >0.8 pixel units in order to prevent the grain boundary reconstruction process from incorporating large unindexed areas. Crystallographic orientations are presented as hemispherical pole figure plots of crystallographic (hkl) planes. For each dataset, maps of band contrast, phase and grain boundaries, and the MTEX property 'mis2mean' (the misorientation of a measurement within a reconstructed grain relative to the mean orientation of all measurements in the grain) are provided in supplemental materials.

3. Geologic setting

In the western Canadian Shield, the >20,000 km^2 Athabasca granulite terrane occurs in the hanging wall of the >500 km-long Legs Lake thrust-sense shear zone in northern Saskatchewan and southeastern Northwest Territories, Canada (Fig. 1A and B; Mahan et al., 2003, 2006; Mahan and Williams, 2005). The terrane is underlain by Archean-Paleoproterozoic felsic and mafic granulites, quartzite, and minor eclogite that equilibrated at >0.6–1.6 GPa (>20-60 km-depths: Dumond et al., 2018, Fig. 1B). Several m-to 100s of km-scale ductile shear zones occur throughout the terrane, including the Wholdaia Lake shear zone (Thiessen et al., 2018), the Cora Lake shear zone (Regan et al., 2014; Orlandini et al., 2019; Orlandini and Mahan, 2020), the Oldman-Bulyea shear zone (Card, 2001; Dumond et al., 2013), and the Grease River shear zone (Fig. 1B; Dumond et al., 2008, 2010; Dumond, 2020). In this contribution, we focus on the Grease Bay segment of the 7 km-thick >400 km-long Grease River shear zone and the 200 m-thick >1 km-long Athabasca Shoreline shear zone that occurs parallel to and

4 km east of the Grease River shear zone (starred locations 04G-029B and 04G-050 along cross-section in Fig. 1C).

4. Structure of deep crustal shear zones in the Athabasca granulite terrane, Saskatchewan, Canada

4.1. Grease River shear zone: Grease Bay, East Lake Athabasca

The Grease River shear zone (GRsz) cuts the Legs Lake shear zone and offsets the Athabasca granulite terrane by 110 km of dextral strike-slip displacement (Fig. 1B; Mahan and Williams, 2005). Several of the best exposures of the GRsz occur in Grease Bay along the north shore of Lake Athabasca (Fig. 2). In this area, the deformed western margin of the calc-alkaline Neoarchean Mary batholith occurs in the footwall of the GRsz (region defined by the blue linework in Fig. 1C; Hanmer, 1994). Rocks within the 5-7 km-thick shear zone include migmatitic paragneisses and felsic granulites (Fig. 2A and C), gray quartzofeldspathic gneisses (Fig. 2B and D-E), and a variety of deformed and undeformed granite dikes. The earliest generation of granite dikes are pegmatitic and highly transposed (Fig. 2D; Dumond et al., 2008). In low strain domains, early gently-dipping gneissic foliations ($S_{0/1}$) and leucosomes in the migmatitic paragneisses are folded into recumbent F_1 folds that are overprinted by a steeply NW-dipping S_2 cleavage defined by biotite and ribbons of quartz and plagioclase (Fig. 2A). This overprinting locally produced Type 3 fold interference patterns with gently SW-plunging intersection lineations defined by S_2 on S_1 (Figs. 1D and 2A). In higher strain domains, F_2 folds become either sheath-like (Fig. 2B) or tight to isoclinal with hinges and intersection lineations that parallel the penetrative L_2 stretching lineation (Fig. 2C; compare F_2 hinges and intersection lineations in Fig. 1D with stretching lineations in Fig. 1E). The predominant mylonitic foliation (S_2) is steeply NW-dipping with a gently SW-plunging stretching lineation defined by quartz and feldspar ribbons and blades of sillimanite (Fig. 1E). Abundant plagioclase, K-feldspar, and garnet σ- and δ-type porphyroclasts in mylonite and ultramylonite gneisses indicate dextral top-to-the-NE shear and oblique thrust-sense in planes observed perpendicular to the foliation and parallel to the stretching lineation (Fig. 2D and E; Dumond, 2020). No consistent sense-of-shear was observed in planes perpendicular to the lineation. The occurrence of ubiquitous steeply-dipping foliations associated with gently-plunging stretching lineations that parallel fold axes and intersection lineations suggests the geometry of transpressive shearing in the GRsz was monoclinic Y_I-type (Passchier, 1998). Previous monazite geochronology applied to syn-kinematic monazite domains revealed episodic shear strain from 1.92 Ga to <1.80 Ga (Dumond et al., 2008; Dumond, 2020).

4.2. Athabasca Shoreline shear zone in the Mary batholith: East Lake Athabasca

Several smaller-scale NE-striking shear zones (10s–100s of m in thickness) occur throughout the Mary batholith east of the GRsz (Fig. 1C and F). Orthogneisses and minor paragneisses in the batholith contain penetrative sub-horizontal gneissic fabrics (S_1) and stretching lineations (L_1) that represent a record of 2.60–2.55 Ga lower crustal flow (D_1) at 0.9 GPa and 800 °C (Figs. 1C and 1G-H; Dumond et al., 2010). Folding of these fabrics produced open to tight F_2 folds with horizontal to gently SW-plunging hinges in the Mary batholith (Figs. 1C and 3A). Hinge regions of these folds less commonly display a well-developed spaced

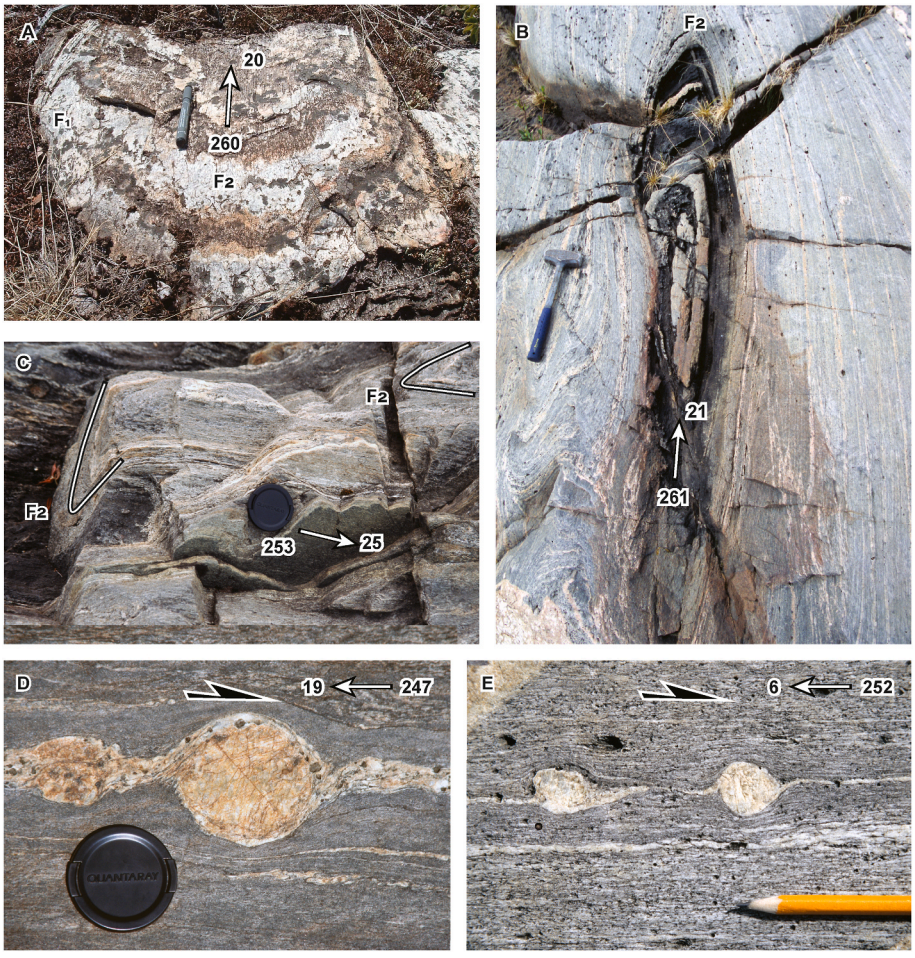

Fig. 2. Field observations from the Grease River shear zone (GRsz). **A)** Type 3 fold interference pattern defined by F_1 recumbent fold of migmatite overprinted by steeply-dipping S_2 cleavage in low strain domain of GRsz. **B)** SW-plunging sheath fold in gray quartzofeldspathic gneiss. **C)** Gently SW-plunging F_2 folds with intersection lineations parallel to the stretching lineation. **D)** Dextral δ-clast derived from a highly transposed granite pegmatite dike. **E)** Ultramylonite zone within the GRsz hosting dextral plagioclase δ-clasts.

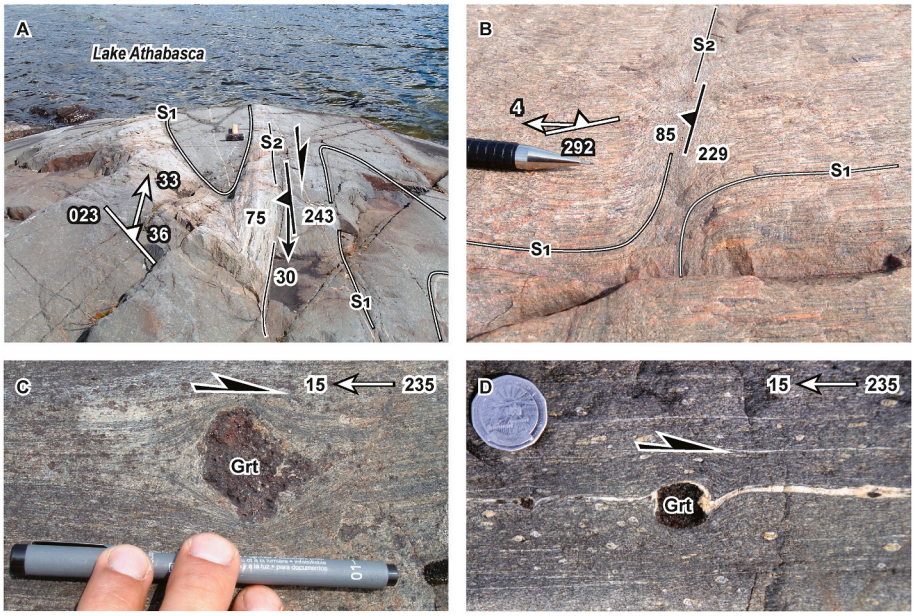

Fig. 3. Field observations adjacent to and within the Athabasca Shoreline shear zone (ASsz). **A)** Tight F_2 fold of S_1 gneissic fabrics within the Turcotte granodiorite in the Mary batholith adjacent to the ASsz. Note minor dextral shear zone that nucleated on the steep limb of the fold. **B)** Example of spaced S_2 cleavage development in the hinge of a km-scale F_2 antiform adjacent to the ASsz. **C)** Garnet porphyroclast in ASsz with intensification of gneissic fabric above and below the clast. Strain shadows define subtle dextral shear sense. **D)** Garnet δ-clast with tails defined by leucosome in an ultramylonite in the ASsz.

cleavage in the granodiorite orthogneisses (Fig. 3B). Locally, D_1 structures are transposed into cm- to 100s of m-thick shear zones characterized by NE-striking mylonite to ultramylonite foliations (S_2) with gently SW-plunging stretching lineations (L_2) (Fig. 1C and F). The majority of these zones display dextral top-to-the-NE kinematics in planes observed perpendicular to the foliation and parallel to the stretching lineation (Fig. 3C and D), although a minor number of conjugate sinistral shear zones are present east of the section depicted in Fig. 1C (Dumond et al., 2010). No consistent sense of shear was observed in planes perpendicular to the lineation. The strike of the 200 m-thick Athabasca Shoreline shear zone (ASsz) is sub-parallel to the GRsz (compare Fig. 1E and F). The ASsz is one of the larger examples of NE-striking dextral shear zones in the Mary batholith that represent strain localization along one limb of a km-scale open F_2 fold (Fig. 1C and 3A). Garnet σ- and δ-clasts observed in paragneisses (Fig. 3C) and in orthogneisses (Fig. 3D) display dextral kinematics. Orthogneisses contain abundant porphyroclasts of lenticular plagioclase and K-feldspar associated with a penetrative straight gneissic fabric (Fig. 3D; Dumond et al., 2010). Previous monazite petrochronology in transposed felsic granulites within the ASsz documented at least one episode of shear strain at 1.92–1.89 Ga based on analysis of syn-kinematic rims associated with Neoarchean monazite grains that grew in the presence of garnet + melt (Dumond et al., 2010; Dumond, 2020).

5. Monazite-bearing L-S tectonites

Penetrative L-S and L > S tectonites occur throughout the GRsz and ASsz. Monazite is most commonly found in garnet-bearing felsic granulites. Felsic granulites throughout the Athabasca granulite terrane are commonly nearly anhydrous (Fig. 4A). In many D_2 high strain zones like the GRsz and ASsz, however, felsic granulites experienced retrogression in the presence of fluid that is commonly manifested as syn- to late-kinematic biotite and muscovite in the presence of texturally resorbed garnet (Fig. 4B–D and 6A; Mahan et al., 2006; Dumond et al., 2013; Leslie et al., 2015). We present data below from the most well-studied felsic granulite sample in each zone.

5.1. Outcrop 04G-29B: retrogressed garnet + sillimanite felsic granulite paragneiss in the GRsz

Felsic granulites in Grease Bay are characterized by a steeply NW-dipping penetrative S_2 gneissic foliation and a gently SW-plunging stretching lineation (Fig. 4E). Major phases are Bt + Ms + Sil + Grt + Kfs + Pl + Qtz with Mnz + Zrn as accessory phases (mineral abbreviations after Bucher and Frey, 2002). At both the outcrop and thin section-scale, the gneissic foliation wraps around elliptical aggregates of garnet + biotite + muscovite with aspect ratios of 1.5–4.8 that define oblique shape-preferred orientations (S_3) trending 009–020°. The aggregates are inferred to be pseudomorphs of originally larger and more spherical garnet porphyroblasts. They are inclined counterclockwise with respect to the main dextral shear fabric (15–45°; Fig. 4B and E). The oblique shape-preferred orientation of the elliptical aggregates was measured in the outcrop for $n = 108$ occurrences on surfaces that were sub-parallel to the stretching lineation and perpendicular to the foliation (Fig. 4B). The aggregates have an average orientation of 28° ± 5° with respect to the foliation and aspect ratios of 2.9 ± 0.7. The penetrative foliation is defined by quartz ribbons and fine grained (10s of μm) recrystallized layers of K-feldspar + plagioclase + quartz (Fig. 4C–E). Stretching parallel to the foliation is indicated by boudinage of sillimanite with prismatic porphyroclasts separated by elongated needles (Fig. 4E; Leslie et al., 2015). Garnet porphyroblasts (3–20 mm in size) are texturally resorbed and fractured with cracks filled or defined by muscovite (Fig. 4C and D). Foliated biotite + muscovite occurs within the strain shadows of garnet, consistent with late syn-S_3 retrogression (Fig. 4C and D).

Several elongate monazite grains (100–220 μm) occur throughout the matrix and have aspect ratios of 1.6–4.6 with long axes oblique (3–27°) to the foliation (Figs. 4E–5). High spatial resolution X-ray maps of these grains reveal 5-40 μm-wide rims defined by Ca or Th and less commonly Y (Figs. 4E and 5). The orientation and core-to-rim compositional zoning in most of these grains is consistent with the rim domains occurring in low strain zones compatible with dextral shear strain, i.e., as strain shadows that developed at low angles with respect to the foliation (e.g., grains m3, m6, and m9 in Figs. 4E and 5A-C; Passchier and Trouw, 2005). Monazite grain m8 may be a δ-clast, with rim domains that developed during rotation concurrent with dextral shear strain. Monazite m8 is the only grain enclosed entirely in quartz, occurring in a F_3 kink band of a quartz-rich layer (Figs. 4E and 5C). Several monazite grains occur in close spatial association with kinematically significant microstructures, including the profound development of boudinage of sillimanite grains parallel to the foliation (Fig. 4E; Leslie et al., 2015). Grain m6 lies directly on top of a sillimanite

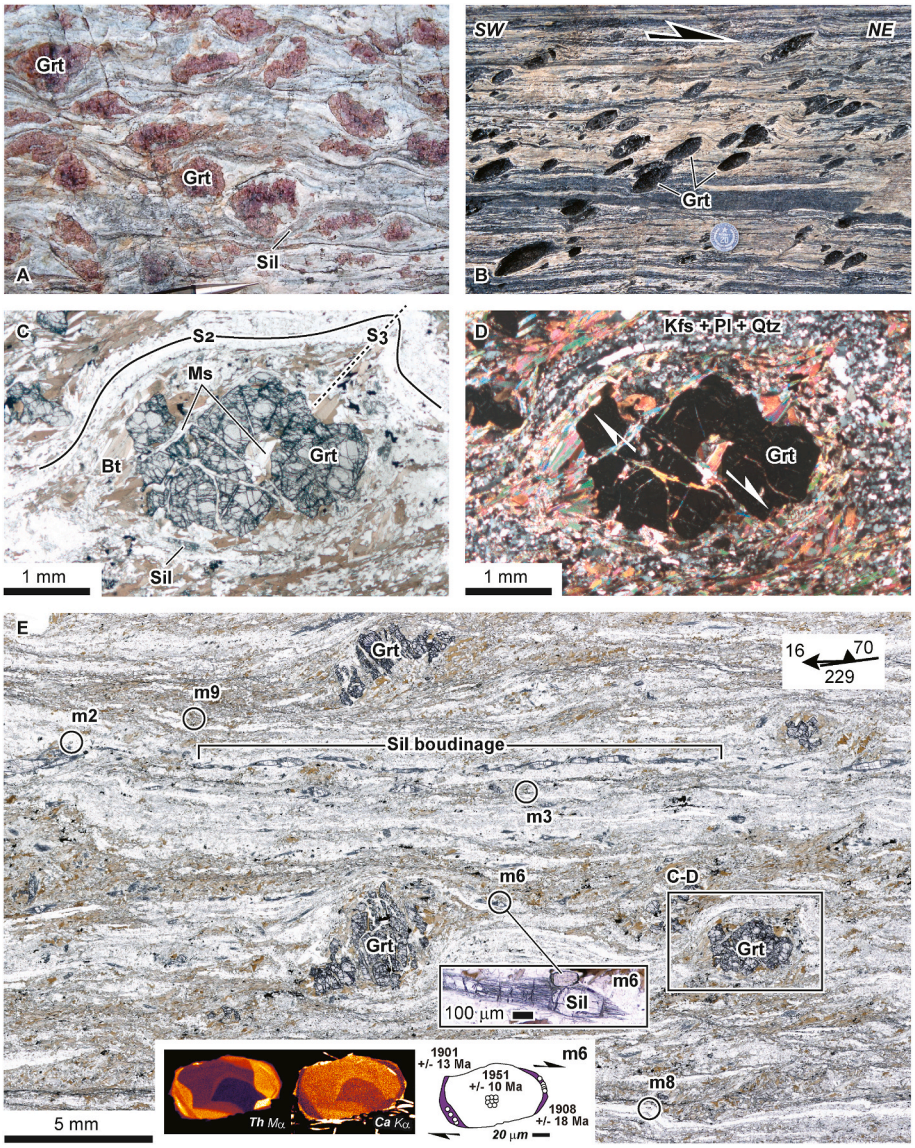

Fig. 4. A) Example of nearly anhydrous felsic granulite from a domain east of the GRsz in the Athabasca granulite terrane. **B)** Example of hydrated felsic granulite in the GRsz at the 04G-029B locality first described by Leslie et al. (2015). Note oblique fabric defined by inclined elliptical clasts of retrogressed garnet consistent with dextral shear sense. **C)** Plane-polarized light photomicrograph of fractured and offset garnet porphyroclast with fractures and strain shadows filled with biotite + muscovite + quartz. Note penetrative S_2 fabric wrapping the clast and buckled by S_3. **D)** Cross-polarized light photomicrograph for region in **C)** indicating the fine grained gneissic S_2 fabric defined by recrystallized plagioclase + K-feldspar + quartz and elongate ribbons of quartz. Note offset of garnet clast. **D)** High resolution scan of thin section showing inclined, resorbed, and fractured garnet clasts with locations of monazite grains analyzed in this study, e.g., m6. Note boudinage of sillimanite across the entire length of the section. Monazite m6 occurs in contact with a stretched sillimanite grain near the strain shadow of a larger garnet clast with Ca-poor rims that define a σ-type geometry consistent with dextral shear sense. Electron microprobe Th–U-Pb dates are indicated.

porphyroclast at the contact between the serrated margin of the clast and the elongate <15 μm-thick needles/tails adjacent to the clast (Fig. 4E).

5.2. *Outcrop 04G-050: retrogressed garnet felsic granulite ultramylonite in the ASsz*

Felsic granulite layers transposed within the fabric of the ASsz in the Mary batholith are ultramylonites and contain Grt + Kfs + Pl + Bt + Qtz with Mnz + Zrn as accessory phases (Fig. 3C and D and 6). Quartz ribbons are elongated parallel to the foliation, and locally extend across the entire length of the thin sections. Grain sizes for recrystallized K-feldspar and plagioclase in the penetrative foliation approach 20 μm. Tens of mm-to 4 cm diameter garnet porphyroclasts have asymmetric strain shadows that define dextral σ-type clasts (Figs. 3C and 6A), whereas garnet clasts in other layers have deformed tails of leucosome that define dextral δ-clasts (Fig. 3D). Garnet is variably retrogressed to an aggregate of biotite + plagioclase + quartz, but like 04G-029B in the GRsz, these garnet aggregates remain largely coherent (Fig. 6A). This is consistent with garnet breakdown occurring late-to post-kinematic.

Several elongate monazite grains occur within the ultramylonite fabric (<40–150 μm; Fig. 6), and rare Neoarchean monazite inclusions have been identified in the larger garnet porphyroclasts (Dumond et al., 2010). The matrix grains have aspect ratios of 1.7–2.8 with long axes oblique (5–26°) to the foliation (Fig. 6). High spatial resolution X-ray maps of these grains reveal 3-30 μm-wide rims defined by Y, Ca, and/or Th (Fig. 6). Other rim domains are as long as 90 μm (grain A-m6 in Fig. 6B). The orientation and core-to-rim compositional zoning in most of these grains is consistent with the rim domains occurring in low strain zones compatible with dextral shear strain, i.e., as strain shadows that developed at low angles with respect to the foliation, similar to monazite grains in 04G-029B from the GRsz (Fig. 6; Passchier and Trouw, 2005). These rim domains mimic the geometry of dextral shear strain defined by the large garnet porphyroclasts with sigmoidal strain shadows, e.g., monazite grain B-m13 in Fig. 6A.

6. Th–U-Pb monazite electron microprobe petrochronology

6.1. *Dates for syn-kinematic monazite rims in the Grease River and Athabasca Shoreline shear zones*

Th–U-Pb dates for syn-kinematic rim domains in both samples are summarized in Fig. 7. The magnitude of the uncertainties on these dates largely depends on the concentrations of Th and U in each compositional

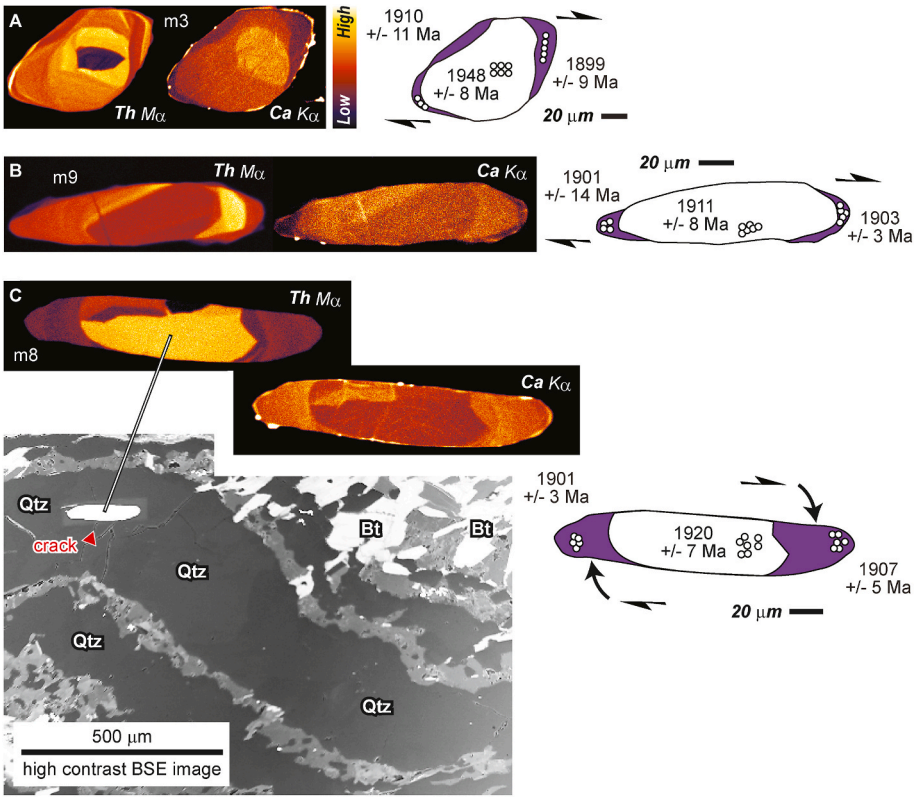

Fig. 5. X-ray maps and Th–U-Pb dates for monazite grains in 04G-029B from the GRsz. Sketches indicate inferred dextral shear sense for each of the dated grains. Note high-contrast BSE (backscattered electron) image of microstructural setting for m8 in an F_3 kink fold.

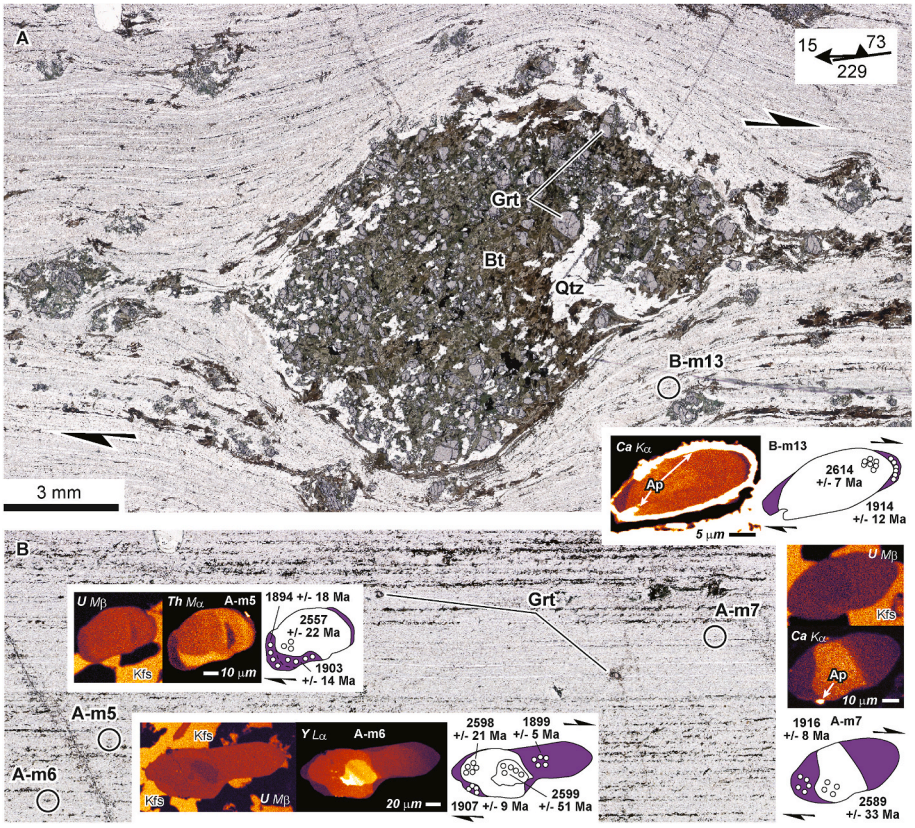

Fig. 6. High resolution scans of thin sections from 04G-050, a garnet-bearing ultramylonite in the Athabasca Shoreline shear zone (ASsz) and X-ray maps with sketches for syn-kinematic monazite grains in both thin sections. Grt = garnet; Bt = biotite; Ap = apatite; Kfs = K-feldspar. **A)** Large dextral garnet σ-clast altered to biotite + quartz in sample taken from outcrop in Fig. 3C. Note location of monazite grain B-m13. **B)** Thin section of ultramylonite sampled in outcrop depicted in Fig. 3D with X-ray maps and sketches of syn-kinematic monazite grains throughout the matrix. Electron microprobe Th–U-Pb dates are indicated.

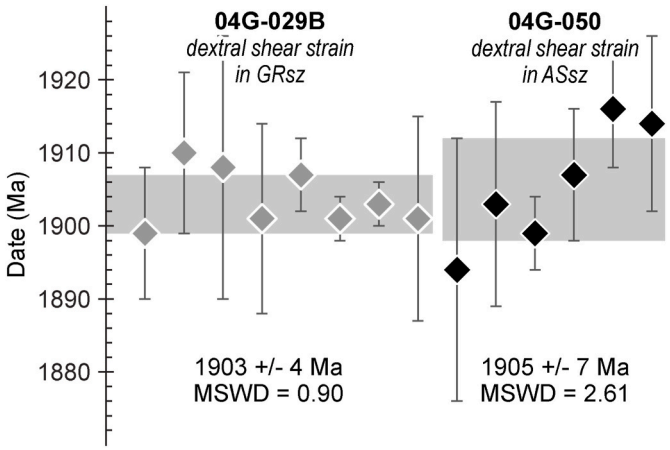

Fig. 7. Vertical 2σ error bar plot summarizing electron microprobe Th–U-Pb dates for syn-kinematic monazite rim domains in the GRsz and ASsz.

domain, compositional homogeneity of the analyzed domain, X-ray counting statistics, and background correction uncertainties (Williams et al., 2006). In this study, 2σ uncertainties were ± 3–18 m.y. for rim domains with dates of 1916–1894 Ma (Table S1). A weighted mean date calculated for 8 syn-kinematic rim domains in sample 04G-029B in the GRsz is 1903 ± 4 Ma (MSWD = 0.90; Fig. 7). A weighted mean date calculated for 6 syn-kinematic rim domains in sample 04G-050 in the ASsz is 1905 ± 7 Ma (MSWD = 2.6; Fig. 7).

6.2. *Monazite compositional domains and implications for petrochronology*

Monazite petrochronology, as applied here, is the use of monazite dates, compositional zoning in X-ray maps, and *in situ* geochemistry to place direct age constraints on petrological and structural processes in tectonites – igneous and metamorphic rocks that evolved synchronously with deformation (Mahan et al., 2006; Dumond et al., 2008; Williams and Jercinovic, 2012; Williams et al., 2017). Variability in monazite composition is explored by converting the electron probe major and trace element data into mole fractions of monazite calculated according to Pyle et al. (2001; see Table S1). Data for samples 04G-029B and 04G-050 are then plotted as a function of $X_{huttonite}$ in Fig. 8. The huttonite component largely reflects variations in Th + Si in monazite whereas the cheralite component ($X_{cheralite}$) records variations in Ca (Fig. 8; huttonite = (Th, U)SiO_4 and cheralite = Ca(Th, U) $(PO_4)_2$).

6.2.1. *Yttrium (Y) in monazite during growth of garnet in the presence of melt*

Felsic granulites within the GRsz and the ASsz (04G-029B and 04G-050), in addition to several domains in the Athabasca granulite terrane are garnet-rich residues formed during a fluid-absent biotite "dehydration" melting reaction (1) biotite + plagioclase + sillimanite + quartz → garnet + K-feldspar + melt, or (2) biotite + plagioclase + quartz → garnet + orthopyroxene + K-feldspar + melt (Le Breton and Thompson, 1988; Vielzeuf and Montel, 1994; Dumond et al., 2018). Monazite exhibits strong depletions in Y when it precipitates during or after the growth of garnet which incorporates Y and the heavy rare earth elements (Bea and Montero, 1999). Garnet and monazite are the only Y-bearing phases in samples 04G-029B and 04G-050. Analyses for all monazite domains in grains from 04G-029B in the GRsz indicate they are Y-depleted, consistent with their growth or reprecipitation in the presence of garnet ± melt (Fig. 8A; Pyle and Spear, 2003; Dumond et al., 2015). Whereas, all 04G-029B monazite must have grown syn-to post-garnet, some 04G-050 monazite domains first record evidence for Y depletion and garnet growth in the Neoarchean (e.g., grain A-m6 in Fig. 6B; Fig. 8B).

6.2.2. *Thorium (Th) and calcium (Ca) in monazite during melt- and fluid-mediated processes*

Thorium distribution in monazite can be attributed to several processes, among others: (1) Th-enrichment due to partitioning of Th into monazite during crystallization from a peraluminous melt (Xing et al., 2013), (2) Th-depletion due to crystallization during melt loss, i.e., less Th-rich melt available for partitioning of Th into monazite (Dumond et al., 2015), and (3) dissolution and reprecipitation of preexisting monazite that redistributes Th + Ca during metasomatism in the presence of alkaline fluids (Harlov et al., 2011). Thorium and calcium zoning commonly (though not always) mimic one another in monazite due to cheralite (or 'brabantite') exchange (Pyle et al., 2001): [Ca (Th, U) REE_{-2}].

Syn-kinematic rims on monazite grains in sample 04G-029B are most commonly slightly enriched in Th and depleted in Ca with respect to core domains (grains m2, m3, m6, and m9 in Figs. 4E, 5A-C, and 8C). Grain m8 is the only grain completely enclosed in quartz and it is the exception, with rims defined by depletions in Th and subtle enrichments in Ca relative to the core that may have been due to growth that occurred syn-to post-melt loss (Figs. 5C and 8C; Dumond et al., 2015). Overall, 04G-029B grains exhibit a pronounced core-to-rim enrichment in Th at 1.91–1.90 Ga (Fig. 8C). Thorium zoning in X-ray maps illustrate lobate high-Th zones that crosscut internal domains, a phenomenon documented experimentally and attributed to fluid-mediated dissolution and reprecipitation of monazite on a volume-for-volume basis, i.e., during metasomatism (Harlov et al., 2011). Syn-kinematic rims for sample 04G-050 are typically depleted in Ca with respect to core domains (grain B-m13 in Fig. 6A and grains A-m6 and A-m7 in Fig. 6B; Fig. 8D). However, rims for one grain also coincide with depletions in Th with respect to the core (grain A-m5 in Fig. 6B) and may be due to growth synchronous with melt loss. Overall, 04G-050 grains exhibit a pronounced core-to-rim depletion in Ca at 1.92–1.89 Ga that may have coincided with late appearance of apatite (B-m13 and A-m7 in Fig. 6A and B; Fig. 8D). Syn-kinematic development of late apatite due to dissolution of high-Ca monazite and reprecipitation of low-Ca monazite has been documented in syn-tectonic leucogranites in the Grease River shear zone (Dumond et al., 2008).

6.2.3. *Lanthanum (La) and Cerium (Ce) in monazite during feldspar recrystallization at 1.92–1.89 Ga*

Feldspars in granulites are typically enriched in light rare earth elements, particularly La + Ce (Bea, 1996; Villaseca et al., 2003). Monazite rim domains in 04G-050 display significant enrichment in La + Ce (Fig. 8F), in contrast to rim domains from 04G-029B (Fig. 8E). This phenomenon has been observed in other domains in the Athabasca granulite terrane, where it has been attributed to incorporation of La + Ce into monazite during dynamic recrystallization of K-feldspar (Dumond et al., 2015). High spatial resolution X-ray maps of U document the occurrence of recrystallized K-feldspar adjacent to monazite rims in sample 04G-050 (Fig. 6B: A-m5, A-m6, and A-m7).

7. Monazite electron backscatter diffraction data

Electron backscatter diffraction data were collected for six monazite grains in 04G-029B and three grains in 04G-050 (Figs. 9 and 10; Table 1). Pole figures for both samples indicate that (100) for most grains is only slightly oblique to the foliation (i.e., the poles to (100) plot at high angles to the foliation plane; Fig. 9), consistent with the orientations of high aspect ratio grains observed in thin section (Figs. 4E, 5-6, and 11). Poles to (010) and (001) also show general alignment in a girdle parallel with the foliation, i.e., the XY-plane of finite strain (Fig. 9A and B). Misorientation maps ('mis2mean') for all grains are displayed in Fig. 10 with the same color scale illustrating the misorientation of a measurement within a reconstructed grain relative to the mean orientation of all measurements in the grain. Maximum misorientations relative to the mean generally occur immediately adjacent to grain

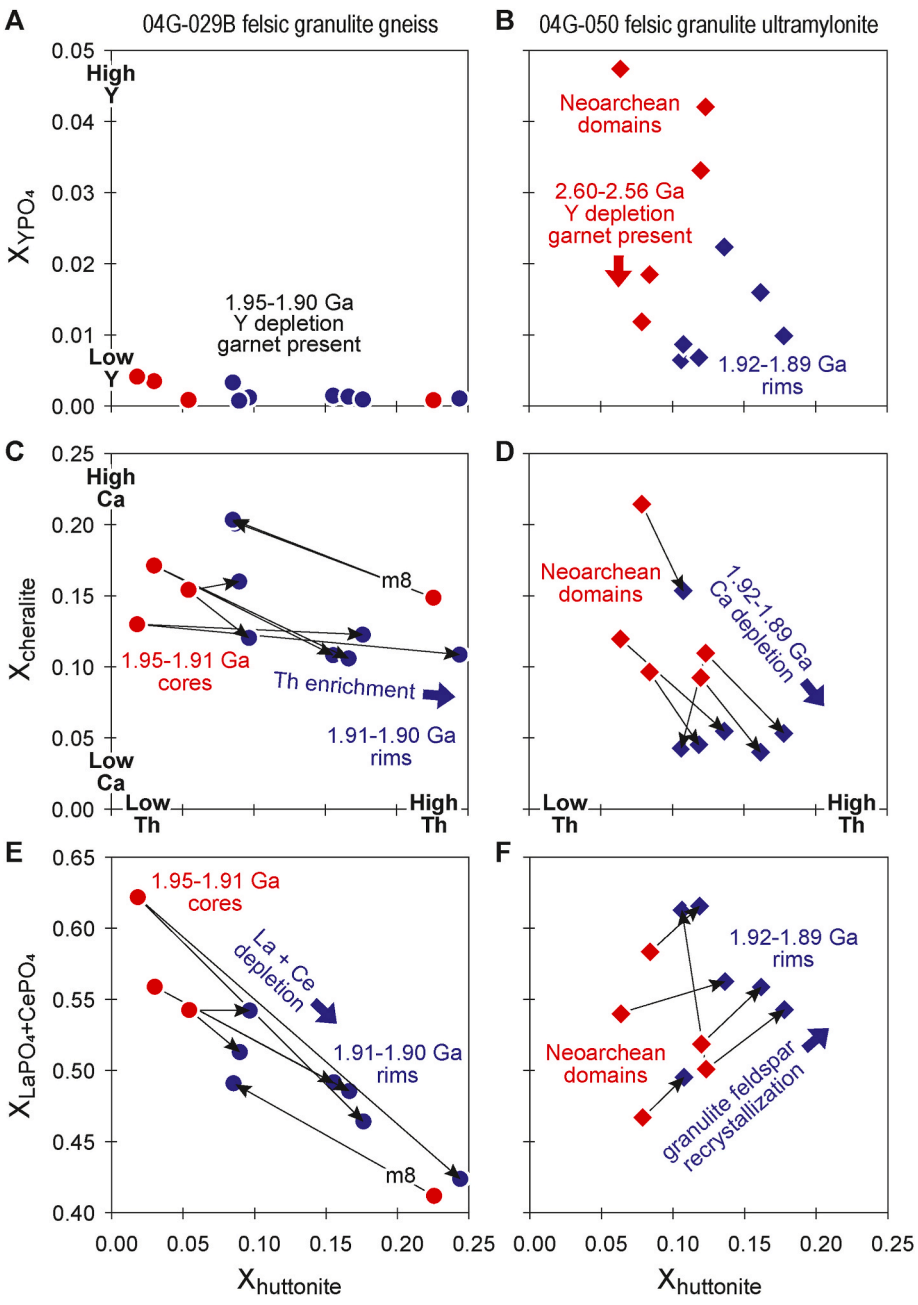

Fig. 8. Monazite petrochronology bivariate plots (**A-F**) summarizing links between monazite dates, core vs. rim compositions, and the inferred processes that produced the compositional domains prior to and during dextral shear strain at 1.92–1.89 Ga. Mole fraction and monazite endmember compositions were calculated according to Pyle et al. (2001) from electron microprobe data in Supplementary Table 1. See text for discussion.

boundaries (Fig. 10) and may be attributed to edge effects related to irregular surface relief where the polished surface is not flat. In a few cases, minor rigid body rotation occurred coincident with cracks in kinks of the S_2 foliation (grain m8 in Figs. 5C, 10E and 10G) or throughgoing cracks across a grain (grain m9 in Fig. 10F and H). The maximum misorientation angles span 1.1–6.9° for all samples, with the majority being <3° (Table 1). These values are small relative to values up to 16° in monazite grains inferred to have experienced crystal plastic deformation (Erickson et al., 2015). An additional measure of internal distortion is the grain orientation spread (GOS), a value that represents the average misorientation relative to the mean. The utility of GOS as a thresholding parameter has been proposed to distinguish dynamically recrystallized quartz grains with low GOS from internally deformed parent grains with high GOS (Cross et al., 2017). Although the threshold values are sample-specific, GOS values for internally deformed quartz grains are commonly much greater than 1° (Cross et al., 2017). With one exception (m8 in Fig. 10E), all monazite grains exhibit a GOS significantly less than 1° (0.26–0.63° in Table 1), suggesting these grains lack internal crystal plastic deformation that could be attributed to dislocation creep.

8. Discussion

Our understanding of shear zone development and evolution in the crust of orogenic belts has focused on the impact of dynamic recrystallization on major rock-forming minerals, e.g., quartz and plagioclase (Hirth and Tullis, 1992; Rybacki and Dresen, 2004). Experimental deformation of granite and felsic gneisses has explored strain localization and deformation mechanisms in poly-phase aggregates (Tullis, 2002; Holyoke and Tullis, 2006). However, there has been

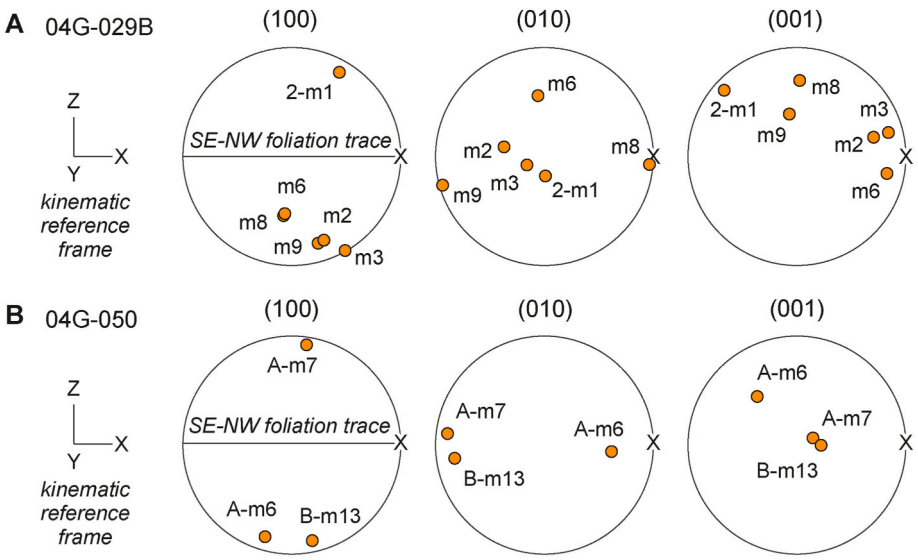

Fig. 9. Pole figures derived from EBSD data for all monazite grains analyzed in this study for **A)** sample 04G-029B in the Grease River shear zone and **B)** sample 04G-050 in the Athabasca Shoreline shear zone. The reference frame for the pole figures is the SW- to NE-striking foliation (traced as a horizontal line) and lineation (labeled as X on plots).

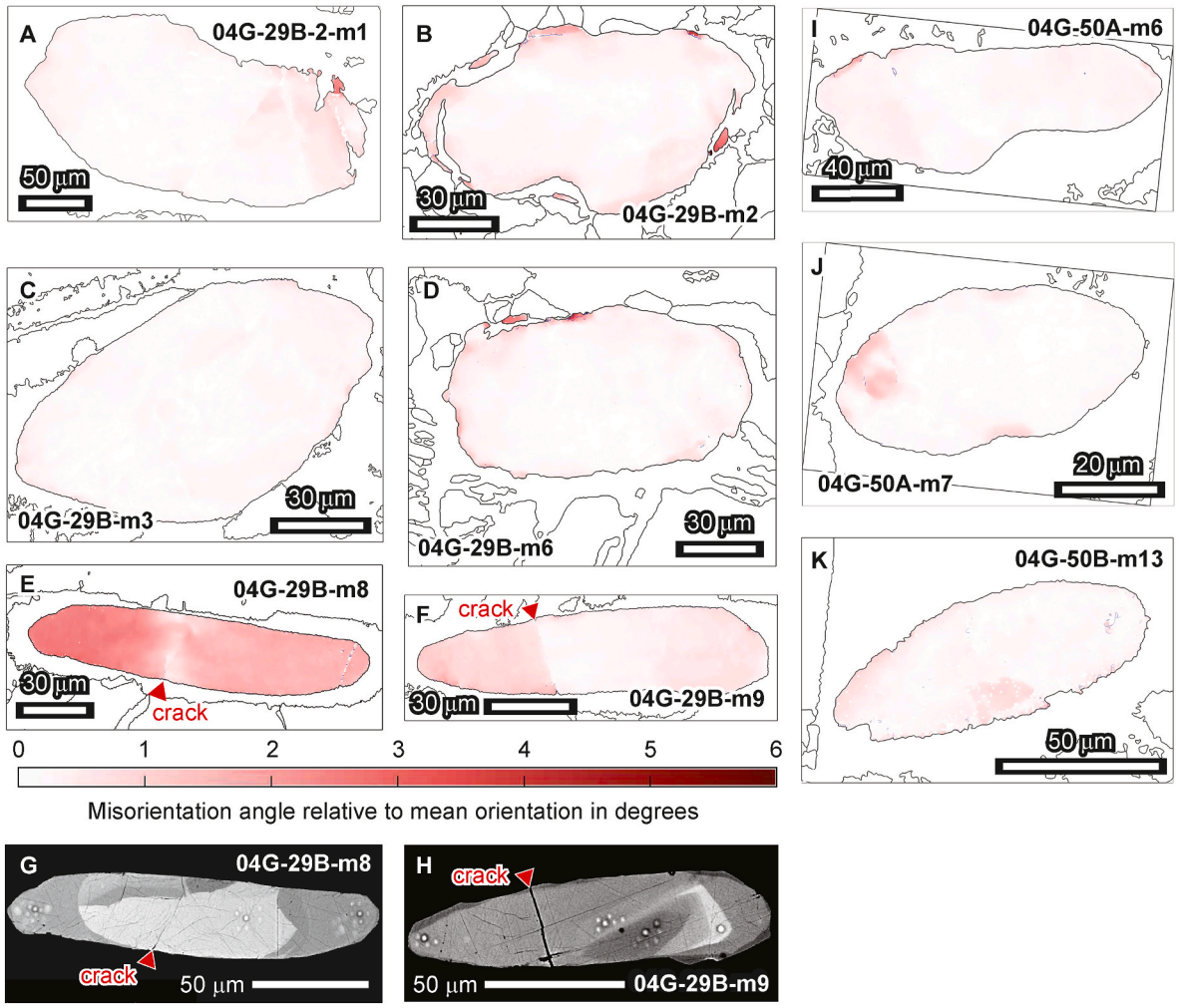

Fig. 10. EBSD misorientation 'mis2mean' maps for all monazite grains in this study **(A-F and I–K)**. Color scale corresponds to degree of misorientation with respect to the mean orientation of all measurements in the grain. Note high-contrast BSE (backscattered electron) images of **G)** monazite grain 04G-029B-m8 and **H)** fractured monazite grain 04G-029B-m9. (For interpretation of the references to color in this figure legend, the reader is referred to the Web version of this article.)

Table 1
EBSD data for monazite grains.[a]

Sample & grain (m#)	map dimensions	map step size (mm)	pixels (raw)	pixels (cleaned)	% retained after cleaning	mean MAD (°) (raw)	mean MAD (°) (cleaned)	mean BC (raw)	mean BC (cleaned)	GOS (°)	max. misorient. (°)
04G-29B-2-m1	234 × 135	1.37	17756	17579	99.0%	0.38	0.36	148	149	0.29	2.6
04G-29B-m2	209 × 131	0.72	13644	13523	99.1%	0.49	0.48	130	130	0.34	6.3
04G-29B-m3	417 × 304	0.32	73270	72599	99.1%	0.46	0.45	120	120	0.26	1.1
04G-29B-m6	256 × 208	0.60	20412	20242	99.2%	0.49	0.48	137	138	0.25	6.9
04G-29B-m8	503 × 220	0.36	36333	35672	98.2%	0.55	0.54	122	123	1.82	3.2
04G-29B-m9	476 × 160	0.30	40850	40261	98.6%	0.47	0.46	108	109	0.63	2.7
04G-50-A-m6	200 × 93	0.93	9906	9763	98.6%	0.52	0.51	132	133	0.35	1.9
04G-50-A-m7	203 × 132	0.36	13085	12853	98.2%	0.45	0.43	134	136	0.30	1.5
04G-50-B-m13	187 × 123	0.63	8110	7508	92.6%	0.71	0.67	119	122	0.47	1.6

[a] Note: Cleaned data had pixels indexed with MAD>1 and grains with less than 5 pixels removed.

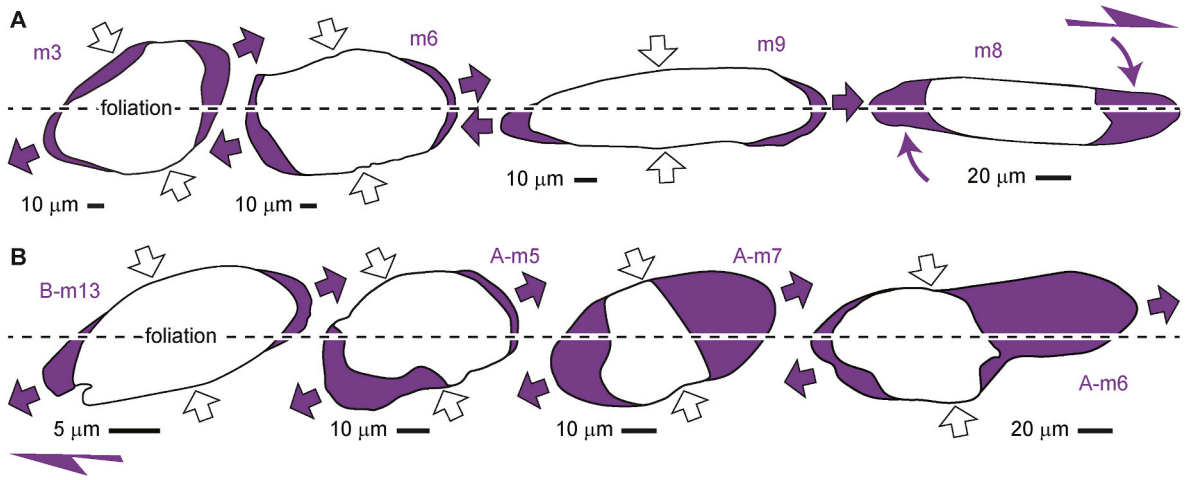

Fig. 11. Line drawings of syn-kinematic monazite grains from **A)** the Grease River shear zone: 04G-029B and **B)** the Athabasca Shoreline shear zone: 04G-050. Note oblique asymmetry of the majority of the grains with respect to the penetrative mylonite fabric with the exception of grain m8 in **A)**. Low angle of obliquity suggests high degree of non-coaxial flow during dextral shear strain and syn-kinematic rim development.

comparatively little work on the impact of shear strain on accessory phases like monazite (Dumond et al., 2008; Wawrzenitz et al., 2012; Erickson et al., 2015). Debate persists regarding the roles of dynamic recrystallization versus dissolution precipitation creep in accommodating deformation of monazite (Wawrzenitz and Krohe, 2016; Erickson et al., 2016). In this study, monazite grains in the penetrative mylonitic fabrics of the GRsz and ASsz appear to provide a valuable textural, compositional, and temporal record of shear strain in felsic granulite gneisses.

The microstructural setting and compositional zoning of the monazite grains provide compelling evidence for syn-kinematic development of monazite rims in low strain domains during dextral shear strain at ~1.90 Ga (Figs. 4–6 and 11). Grains consistently have multi-stage rims that developed progressively in the extensional quadrants of dextral shear strain with respect to the foliation (e.g., Figs. 4E, 5A-C, 6A-B, and 11). One grain displays curved rim domains compatible with dextral rotation of the clast during rim development and may represent a δ-type clast (Figs. 5C, 10G and 11B). The low angle of obliquity (3–27°) for all grains with respect to the foliation may indicate that rim development occurred as a consequence of sub-simple shear strain during non-coaxial flow (Passchier, 1987). These observations demand an explanation for how syn-kinematic monazite domains form in a matrix of quartz and feldspar undergoing grain size reduction via dynamic recrystallization (i.e., Platt and Behr, 2011).

From EBSD data, average monazite grain misorientations relative to the mean grain orientations are typically less than 1° and consistent with no significant dislocation-accommodated internal deformation (Table 1). Comparison of monazite compositional maps (Figs. 4–6) with EBSD maps for misorientation angle (Fig. 10) demonstrates that all of the different compositional domains share the same crystallographic orientation in each grain. These observations are most consistent with a dissolution precipitation creep mechanism rather than some form of dislocation creep-accommodated internal deformation, i.e., Wawrzenitz et al. (2012). We infer that this was facilitated by strain-enhanced dissolution process whereby monazite reprecipitates in low strain extensional domains during strain (e.g., Wintsch and Yi, 2002). There is a growing body of research demonstrating the susceptibility of monazite to dissolution-reprecipitation in the presence of alkaline fluids (Seydoux-Guillaume et al., 2002; Hetherington et al., 2010; Harlov et al., 2011; Williams et al., 2011). This implies that the syn-kinematic monazite rims observed in these tectonites are not strictly overgrowths but instead formed by fluid-mediated coupled

dissolution–precipitation that resulted in a metasomatic volume-for-volume replacement of older monazite domains with monazite of a new composition during ductile shear strain (i.e., Harlov et al., 2005, 2011). Leslie et al. (2015) identified evidence for fluid-mediated dissolution precipitation creep in sillimanite in the sample from the same 04G-029B locality (e.g., sillimanite adjacent to m6 and sillimanite boudinage across the section in Fig. 4E), supporting the impact of this process on other phases at the sample-scale. The data are most consistent with dissolution precipitation creep being the dominant deformation mechanism which produced compositionally-defined domains that reprecipitated in low strain domains compatible with the dextral shear sense observed in thin section and outcrop (Fig. 11). Thus, the monazite rim domains developed during non-coaxial flow as dextral shear strain was accumulating (Fig. 11).

9. Conclusions

Our results indicate that monazite grains in mylonite gneisses provide an important textural and temporal record of shear strain. Compositional X-ray mapping and EBSD data demonstrate that syn-kinematic monazite rims develop in low strain extensional domains via dissolution precipitation creep. Dates of these domains thus provide direct ages of shear zone displacement. The dates and orientations of monazite core and syn-kinematic rim domains may also be used to directly constrain kinematic vorticity in a shear zone, though a statistically large enough population of grains would be required to make this tractable, i.e., Jessup et al. (2007). We suggest *in situ* dating of shear strain with monazite provides a reliable tool for constraining the temporal evolution of strain variability in orogens explored by Ramsay and Graham (1970). In this example, dates for dextral shear strain for both samples overlap within uncertainty (Fig. 7), suggesting that slip along both shear zones was contemporaneous. We conclude that syn-kinematic monazite domains in high temperature shear zones provide absolute ages for episodes of strain accumulation and can directly constrain μm-to km-scale kinematics in continental orogens.

Credit author statement

Gregory Dumond: Conceptualization, Field Mapping, Petrology, Electron Probe and Scanning Electron Microscope Analysis, Writing – Original Draft, Funding Acquisition; **Kevin H. Mahan:** Field Mapping, EBSD and Scanning Electron Microscope Analysis, Writing – Review & Editing, Funding Acquisition; **Philippe Goncalves:** Field Mapping, Petrology, Writing – Review & Editing; **Michael L. Williams:** Field Mapping, Electron Probe Microanalysis, Writing – Review & Editing, Funding Acquisition; **Michael J. Jercinovic:** Electron Probe Microanalysis, Writing – Review & Editing.

Declaration of competing interest

The authors declare that they have no known competing financial interests or personal relationships that could have appeared to influence the work reported in this paper.

Acknowledgements

This manuscript is dedicated to Professor Samuel A. Bowring (1953–2019; Massachusetts Institute of Technology), whose friendship, encouragement, and steadfast support of electron probe monazite petrochronology are profoundly missed. We sincerely appreciate the opportunity to honor the memory of Professor John G. Ramsay (1931–2021), whose pioneering work on shear zones inspired this research. Field support by Scott's General Store and Transwest Airlines in Stony Rapids, Saskatchewan, Canada is gratefully acknowledged. We thank Dr. Tomoko Borsa for outstanding assistance at the COSINC SEM facility. We are grateful for Dr. Micah Jessup's feedback on kinematic analysis of shear zones. We thank Dr. Timmons Erickson for providing the monazite match unit file used for EBSD analysis in this study. Funding was provided by U.S. National Science Foundation grants EAR-0310004, -0609935, −1252295, and −1255277. The stereonets in Fig. 1 were created using GEOrient v. 9.5.0 by Dr. Rod Holcombe. We are grateful for constructive and helpful reviews from Dr. Daniel Harlov, an anonymous reviewer, and guest editor Professor Djordje Grujic that significantly improved the presentation.

Appendix A. Supplementary data

Supplementary data to this article can be found online at https://doi.org/10.1016/j.jsg.2022.104672.

References

Allaz, J.M., Williams, M.L., Jercinovic, M.J., Goemann, K., Donovan, J., 2019. Multipoint Background Analysis: Gaining Precision and Accuracy in Microprobe Trace Element Analysis: Microscopy and Microanalysis, pp. 1–17.

Andronicos, C.L., Hollister, L.S., Davidson, C., Chardon, D., 1999. Kinematics and tectonic significance of transpressive structures within the Coast Plutonic Complex. British Columbia: J. Struct. Geol. 21, 229–243.

Andronicos, C.L., Velasco, A.A., Hurtado, J.M., 2007. Large-scale deformation in the India-Asia collision constrained by earthquakes and topography. Terra. Nova 19, 105–119.

Bajolet, F., Chardon, D., Martinod, J., Gapais, D., Kermarrec, J.-J., 2015. Synconvergence flow inside and at the margin of orogenic plateaus: lithospheric-scale experimental approach. J. Geophys. Res. Solid Earth 120, 6634–6657.

Bea, F., 1996. Residence of REE, Y, Th, and U in granites and crustal protoliths: implications for the chemistry of crustal melts. J. Petrol. 37, 521–552.

Bea, F., Montero, P., 1999. Behavior of accessory phases and redistribution of Zr, REE, Y, Th, and U during metamorphism and partial melting of metapelites in the lower crust: an example from the Kinzigite Formation of Ivrea-Verbano. NW Italy: Geochem. Cosmochim. Acta 63, 1133–1153.

Beaudoin, A., Scaillet, S., Mora, N., Jolivet, L., Augier, R., 2021. In Situ and Step-Heating 40Ar/39Ar Dating of White Mica in Low-Temperature Shear Zones (Tenda Massif, Alpine Corsica, France): Tectonics, vol. 39, e2020TC006246.

Bergemann, C.A., Gnos, E., Berger, A., Whitehouse, M.J., Mullis, J., Walter, F., Bojar, H.-P., 2018. Constraining long-term fault activity in the brittle domain through in situ dating of hydrothermal monazite. Terra. Nova 30, 440–446.

Berger, A., Gnos, E., Janots, E., Whitehouse, M., Soom, M., Frei, R., Waight, T.E., 2013. Dating brittle tectonic movements with cleft monazite: fluid-rock interaction and formation of REE minerals. Tectonics 32, 1176–1189.

Bucher, K., Frey, M., 2002. Petrogenesis of Metamorphic Rocks. Springer, Berlin, p. 341.

Bürgmann, R., Dresen, G., 2008. Rheology of the lower crust and upper mantle: evidence from rock mechanics, geodesy, and field observations. Annu. Rev. Earth Planet Sci. 36, 531–567.

Card, C.D., 2001. Geology and Tectonic Setting of the Oldman-Bulyea Shear Zone, Northern Saskatchewan. M.S. thesis. Regina, University of Regina, Canada.

Ceccato, A., Goncalves, P., Pennacchioni, G., 2020. Temperature, fluid content and rheology of localized ductile shear zones in subsolidus cooling plutons. J. Metamorph. Geol. 38, 881–903.

Cliff, R.A., Meffan-Main, S., 2003. Evidence from Rb-Sr microsampling geochronology for the timing of alpine deformation in the sonnblick dome, SE tauern window, Austria. In: Vance, D., Muller, W., Villa, I.M. (Eds.), Geochronology: Linking the Isotopic Record with Petrology and Textures, vol. 220. The Geological Society, London, pp. 159–172.

Cottle, J., Lederer, G., Larson, K., 2019. The monazite record of pluton assembly: mapping Manaslu using petrochronology. Chem. Geol. 530 article 119309.

Cottle, J.M., Searle, M.P., Jessup, M.J., Crowley, J.L., Law, R.D., 2015. Rongbuk re-visited: geochronology of leucogranites in the footwall of the south Tibetan detachment system, everest region. Southern Tibet: Lithos 227, 94–106.

Cross, A.J., Prior, D.J., Stipp, M., Kidder, S., 2017. The recrystallized grain size piezometer for quartz: an EBSD-based calibration. Geophys. Res. Lett. 44, 6667–6674.

Dumond, G., 2020. Tibetan dichotomy exposed in the Canadian Shield: a lower crustal perspective. Earth Planet Sci. Lett. 544, 116375.

Dumond, G., Goncalves, P., Williams, M.L., Jercinovic, M.J., 2015. Monazite as a monitor of melting, garnet growth and feldspar recrystallization in continental lower crust. J. Metamorph. Geol. 33, 735–762.

Dumond, G., Goncalves, P., Williams, M.L., Jercinovic, M.J., 2010. Subhorizontal fabric in exhumed continental lower crust and implications for lower crustal flow: Athabasca granulite terrane, western Canadian Shield. Tectonics 29, TC2006. https://doi.org/10.1029/2009TC002514.

Dumond, G., Mahan, K.H., Williams, M.L., Jercinovic, M.J., 2013. Transpressive uplift and exhumation of continental lower crust revealed by synkinematic monazite reactions. Lithosphere 5, 507–512.

Dumond, G., McLean, N., Williams, M.L., Jercinovic, M.J., Bowring, S.A., 2008. High-resolution dating of granite petrogenesis and deformation in a lower crustal shear zone: Athabasca granulite terrane, western Canadian Shield. Chem. Geol. 254, 175–196.

Dumond, G., Williams, M.L., Baldwin, J.A., Jercinovic, M.J., 2017. Backarc origin for Neoarchean ultrahigh-temperature metamorphism, eclogitization, and orogenic root growth. Geology 45, 943–946.
Dumond, G., Williams, M.L., Regan, S.P., 2018. The Athabasca granulite terrane and evidence for dynamic behavior of lower continental crust. Annu. Rev. Earth Planet Sci. 46, 353–386.
Erickson, T.M., Pearce, M.A., Taylor, R.J.M., Timms, N.E., Clark, C., Reddy, S.M., Buick, I.S., 2015. Deformed monazite yields high-temperature tectonic ages. Geology 43, 383–386.
Erickson, T.M., Reddy, S.M., Timms, N.E., Pearce, M.A., Taylor, R.J.M., Clark, C., Buick, I.S., 2016. Deformed monazite yields high temperature tectonic ages. Reply: Geology 44, e378.
Fitz-Diaz, E., Cottle, J.M., Vidal-Reyes, M.I., Van der Pluijm, B.A., 2019. In situ Th/Pb dating of monazite in fibrous veins: direct dating of veins and deformation in the shallow upper crust of the Mexican Orogen. J. Struct. Geol. 124, 136–142.
Fletcher, I.R., McNaughton, N.J., Davis, W.J., Rasmussen, B., 2010. Matrix effects and calibration limitations in ion probe U–Pb and Th–Pb dating of monazite. Chem. Geol. 270, 31–44.
Fossen, H., Cavalcante, G.C.G., 2017. Shear zones – a review. Earth Sci. Rev. 171, 434–455.
Gasquet, D., Bertrand, J.-M., Paquette, J.-L., Lehmann, J., Ratzov, G., de Ascenção Guedes, R., Tiepolo, M., Boullier, A.-M., Scaillet, S., Nomade, S., 2010. Miocene to Messinian deformation and hydrothermal activity in a pre-Alpine basement massif of the French western Alps: new U–Th–Pb and Ar ages from the Lauzière massif. Bull. Soc. Geol. Fr. 181, 227–241.
Gnos, E., Mullis, J., Ricchi, E., Bergemann, C.A., Janots, E., Berger, A., 2021. Episodes of fissure formation in the Alps: connecting quartz fluid inclusion, fissure monazite age, and fissure orientation data. Swiss J. Geosci. 114, 14.
Gordon, S.M., Kirkland, C.L., Reddy, S.M., Blatchford, H.J., Whitney, D.L., Teyssier, C., Evans, N.J., McDonald, B.J., 2021. Deformation-enhanced recrystallization of titanite drives decoupling between U-Pb and trace elements. Earth Planet Sci. Lett. 560, 116810.
Grujic, D., Hollister, L.S., Parrish, R.R., 2002. Himalayan metamorphic sequence as an orogenic channel: insight from Bhutan. Earth Planet Sci. Lett. 198, 177–191.
Hanmer, S., 1994. Geology, East Athabasca Mylonite Triangle, Saskatchewan: Map 1859A, Scale 1:100000. Geological Survey of Canada.
Harlov, D.E., Wirth, R., Förster, H.J., 2005. An experimental study of dissolution-reprecipitation in fluorapatite: fluid infiltration and the formation of monazite. Contrib. Mineral. Petrol. 150, 268–286.
Harlov, D.E., Wirth, R., Hetherington, C.J., 2011. Fluid-mediated partial alteration in monazite: the role of coupled dissolution-reprecipitation in element redistribution and mass transfer. Contrib. Mineral. Petrol. 162, 329–348.
Hetherington, C.J., Harlov, D.E., Budzyn, B., 2010. Experimental metasomatism of monazite and xenotime: mineral stability. REE mobility and fluid composition: Mineral. Petrol. 99, 165–184.
Hielscher, R., Schaeben, H., 2008. A novel pole figure inversion method: specification of the MTEX algorithm. J. Appl. Crystallogr. 41, 1024–1037.
Hirth, G., Tullis, J., 1992. Dislocation creep regimes in quartz aggregates. J. Struct. Geol. 14, 145–159.
Holyoke III, C.W., Tullis, J., 2006. Formation and maintenance of shear zones. Geology 34, 105–108.
Hueck, M., Wemmer, K., Basei, M.A.S., Philipp, R.P., Oriolo, S., Heidelbach, F., Oyhantcabal, P., Siegesmund, S., 2020. Dating recurrent shear zone activity and the transition from ductile to brittle deformation: white mica geochronology applied to the Neoproterozoic Dom Feliciano Belt in South Brazil. J. Struct. Geol. 141, 104199.
Jabaloy-Sánchez, A., Azdimousa, A., Booth-Rea, G., Asebriy, L., Vázquez-Vílchez, M., Mártinez- Mártinez, J.M., Gabites, J., 2015. The structure of the Temsamane fold-and-thrust stack (eastern Rif, Morocco): evolution of a transpressional orogenic wedge. Tectonophysics 663, 150–176.
Jannin, S., Gervais, F., Moukhsil, A., Auglund, L.E., 2018. Late-grenvillian channel flow in the central grenville province (manicouagan reservoir area): new constraints from a structural and geochronological study of the allochthon boundary thrust. J. Struct. Geol. 115, 132–151.
Jeanneret, P., Goncalves, P., Durand, C., Poujol, M., Trap, P., Marquer, D., Quirt, D., Ledru, P., 2017. Geochronological constraints on the trans-Hudsonian tectono-metamorphic evolution of the pre-Athabasca basement within the Wollaston-Mudjatik Transition Zone, Saskatchewan. Precambrian Res. 301, 152–178.
Jercinovic, M.J., Williams, M.L., Lane, E.D., 2008. In-situ trace element analysis of monazite and other fine-grained accessory minerals by EPMA. Chem. Geol. 254, 197–215.
Jessup, M.J., Law, R.D., Frassi, C., 2007. The Rigid Grain Net (RGN): an alternative method for estimating mean kinematic vorticity number (Wm). J. Struct. Geol. 29, 411–421.
Krohe, A., Wawrzenitz, N., 2000. Domainal variations of U–Pb monazite ages and Rb–Sr whole rock dates in polymetamorphic paragneisses (KTB Drill Core, Germany): influence of strain and deformation mechanisms on isotope systems. J. Metamorph. Geol. 18, 271–291.
Kylander-Clark, A.R.C., Hacker, B.R., Cottle, J.M., 2013. Laser-ablation split-stream ICP petrochronology. Chem. Geol. 345, 99–112.
Langille, J.M., Jessup, M.J., Cottle, J.M., Lederer, G., Ahmad, T., 2012. Timing of metamorphism, melting and exhumation of the Leo Pargil dome, northwest India. J. Metamorph. Geol. 30, 769–791.
Le Breton, N., Thompson, A.B., 1988. Fluid-absent (dehydration) melting of biotite in metapelites in the early stages of crustal anatexis. Contrib. Mineral. Petrol. 99, 226–237.
Lederer, G.W., Cottle, J.M., Jessup, M.J., Langille, J.M., Ahmad, T., 2013. Timescales of partial melting in the Himalayan middle crust: insight from the Leo Pargil dome, northwest India. Contrib. Mineral. Petrol. 166, 1415–1441.
Leslie, S.R., Mahan, K.H., Regan, S., Williams, M.L., Dumond, G., 2015. Contrasts in sillimanite deformation in felsic tectonites from anhydrous granulite- and hydrous amphibolite-facies shear zones, western Canadian Shield. J. Struct. Geol. 71, 112–124.
Lin, Y.L., Lee, T.Y., Lo, C.H., Sherlock, S.C., Iizuka, Y., Usuki, T., Quek, L.X., Charusiri, P., 2021. Dating deformation using sheared leucogranite: temporal constraints by 40Ar/39Ar thermochronology for the Mae Ping shear zone. NW Thailand: Contrib. Mineral. Petrol. 176, 65.
Mahan, K.H., Goncalves, P., William, M.L., Jercinovic, M.J., 2006. Dating metamorphic reactions and fluid flow: application to exhumation of high-P granulites in a crustal-scale shear zone, western Canadian Shield. J. Metamorph. Geol. 24, 193–217.
Mahan, K.H., Williams, M.L., 2005. Reconstruction of a large deep-crustal terrane: implications for the Snowbird tectonic zone and early growth of Laurentia. Geology 33, 385–388.
Mahan, K.H., Williams, M.L., Baldwin, J.A., 2003. Contractional uplift of deep crustal rocks along the Legs Lake shear zone, western Churchill Province, Canadian Shield. Can. J. Earth Sci. 40, 1085–1110.
Mainprice, D., Bachmann, F., Hielscher, R., Schaeben, H., 2014. Descriptive tools for the analysis of texture projects with large datasets using MTEX: strength, symmetry and components. In: Faulkner, D.R., Mariani, E., Mecklenburgh, J. (Eds.), Rock Deformation from Field, Experiments and Theory: A Volume in Honour of Ernie Rutter, vol. 409. Geological Society, London. https://doi.org/10.1144/SP409.8.
Orlandini, O.F., Mahan, K.H., 2020. Rheological evolution of a pseudotachylyte-bearing deep crustal shear zone in the western Canadian Shield. J. Struct. Geol. 141 https://doi.org/10.1016/j.jsg.2020.104188.
Orlandini, O.F., Mahan, K.H., Williams, M.J., Regan, S.P., Mueller, K.J., 2019. Evidence for deep crustal seismic rupture in a granulite-facies, intraplate, strike-slip shear zone, northern Saskatchewan. Canada: Geol. Soc. Am. Bull. 131, 403–425.
Paquette, J.L., Tiepolo, M., 2007. High resolution (5 μm) U-Th-Pb isotope dating of monazite with excimer laser abaltion (ELA)-ICPMS. Chem. Geol. 240, 222–237.
Passchier, C.W., 1987. Stable positions of rigid objects in non-coaxial flow—a study in vorticity analysis. J. Struct. Geol. 9, 679–690.
Passchier, C.W., 1998. Monoclinic model shear zones. J. Struct. Geol. 20, 1121–1137.
Passchier, C.W., Trouw, R.A.J., 2005. Micro-tectonics, second ed. Springer, Berlin, p. 366.
Platt, J.P., Behr, W.M., 2011. Grainsize evolution in ductile shear zones: implications for strain localization and the strength of the lithosphere. J. Struct. Geol. 33, 537–550.
Pyle, J.M., Spear, F.S., 2003. Four generations of accessory-phase growth in low-pressure migmatites from SW New Hampshire. Am. Mineral. 88, 338–351.
Pyle, J.M., Spear, F.S., Rudnick, R.L., McDonough, W.F., 2001. Monazite-Xenotime-garnet equilibrium in metapelites and a new monazite-garnet thermometer. J. Petrol. 42, 2083–2107.
Ramsay, J.G., Graham, R.H., 1970. Strain variation in shear belts. Can. J. Earth Sci. 7, 786–813.
Ramsay, J.G., 1980. Shear zone geometry: a review. J. Struct. Geol. 2, 83–99.
Regan, S.P., Williams, M.L., Leslie, S., Mahan, K.H., Jercinovic, M.J., Holland, M.E., 2014. The Cora Lake shear zone, Athabasca granulite terrane, an intraplate response to far- field orogenic processes during the amalgamation of Laurentia. Can. J. Earth Sci. 51, 877–901.
Rybacki, E., Dresen, G., 2004. Deformation mechanism maps for feldspar rocks. Tectonophysics 382, 173–187.
Sassier, C., Leloup, P.H., Rubatto, D., Galland, O., Yue, Y., Lin, D., 2009. Direct measurement of strain rates in ductile shear zones: a new method based on syntectonic dikes. J. Geophys. Res. Solid Earth 114, 22.
Seydoux-Guillaume, A.-M., Paquette, J.-L., Wiedenbeck, M., Montel, J.-M., Heinrich, W., 2002. Experimental resetting of the U-Th-Pb systems in monazite. Chem. Geol. 191, 165–181.
Shaw, C.A., Karlstrom, K.E., Williams, M.L., Jercinovic, M.J., McCoy, A.M., 2001. Electron- microprobe monazite dating of ca. 1.71-1.63 Ga and ca. 1.45-1.38 Ga deformation in the Homestake shear zone, Colorado. Origin and early evolution of a persistent intracontinental tectonic zone: Geology 29, 739–742.
Storey, C.D., Brewer, T.S., Parrish, R.R., 2004. Late-Proterozoic tectonics in northwest Scotland: one contractional orogeny or several? Precambrian Res. 134, 227–247.
Thiessen, E.J., Gibson, H.D., Regis, D., Pehrsson, S.J., 2018. Deformation and extensional exhumation of 1.9 Ga high-pressure granulites along the Wholdaia Lake shear zone, south Rae craton, Northwest Territories. Canada: Lithosphere 10, 641–661.
Thigpen, J.R., Law, R.D., Loehn, C.L., Strachan, R.A., Tracy, R.J., Lloyd, G.E., Roth, B.L., Brown, S.J., 2013. Thermal structure and tectonic evolution of the Scandian orogenic wedge, Scottish Caledonides: integrating geothermometry, deformation temperatures and conceptual kinematic-thermal models. J. Metamorph. Geol. 31, 813–842.
Tikoff, B., de Saint Blanquat, M., 1997. Transpressional shearing and strike-slip partitioning in the Late Cretaceous Sierra Nevada magmatic arc. California: Tectonics 16, 442–459.
Tullis, J., 2002. Deformation of granitic rocks: experimental studies and natural examples. In: Karato, S., Wenk, H.-R. (Eds.), Reviews in Mineralogy and Geochemistry, vol. 51. Mineralogical Society of America, Washington, D.C., pp. 51–96
Vielzeuf, D., Montel, J.M., 1994. Partial melting of metagreywackes. Part I. Fluid-absent experiments and phase relationships. Contrib. Mineral. Petrol. 117, 375–393.
Villaseca, C., Romera, C.M., De la Rosa, J., Barbero, L., 2003. Residence and redistribution of REE, Y, Zr, Th and U during granulite-facies metamorphism:

behaviour of accessory and major phases in peraluminous granulites of central Spain. Chem. Geol. 200, 293–323.
Warren, C.J., Greenwood, L.V., Argles, T.W., Roberts, N.M.W., Parrish, R.R., Harris, N.B. W., 2018. Garnet–monazite rare earth element relationships in sub-solidus metapelites: a case study from Bhutan. In: Ferrero, S., Lanari, P., Goncalves, P., Grosch, E.G. (Eds.), Metamorphic Geology: Microscale to Mountain Belts, vol. 478. Geological Society, London. https://doi.org/10.1144/SP478.1.
Wawrzenitz, N., Krohe, A., Rhede, D., Romer, R.L., 2012. Dating rock deformation with monazite: the impact of dissolution precipitation creep. Lithos 134–135, 52–74.
Wawrzenitz, N., Krohe, A., Baziotis, I., Mposkos, E., Kylander-Clark, A.R.C., Romer, R.L., 2015. LASS U–Th–Pb monazite and rutile geochronology of felsic high-pressure granulites (Rhodope, N Greece): effects of fluid, deformation and metamorphic reactions in local subsystems. Lithos 232, 266–285.
Wawrzenitz, N., Krohe, A., 2016. Deformed monazite yields high-temperature tectonic ages. Comment: Geology 44, e378.
Williams, M.L., Jercinovic, M.J., 2002. Microprobe monazite geochronology: putting absolute time into microstructural analysis. J. Struct. Geol. 24, 1013–1028.
Williams, M.L., Jercinovic, M.J., 2012. Tectonic interpretation of metamorphic tectonites: integrating compositional mapping, microstructural analysis, and in situ monazite dating. J. Metamorph. Geol. 30, 739–752.
Williams, M.L., Jercinovic, M.J., Goncalves, P., Mahan, K., 2006. Format and philosophy for collecting, compiling, and reporting microprobe monazite ages. Chem. Geol. 225, 1–15.
Williams, M.L., Jercinovic, M.J., Harlov, D.E., Budzyn, B., Hetherington, C.J., 2011. Resetting monazite ages during fluid-related alteration. Chem. Geol. 283, 218–225.
Williams, M.L., Jercinovic, M.J., Mahan, K.H., Dumond, G., 2017. Electron microprobe petrochronology. Rev. Mineral. Geochem. 83, 153–182.
Williams, M.L., Jercinovic, M.J., Terry, M.P., 1999. Age mapping and dating of monazite on the electron microprobe: deconvoluting multistage tectonic histories. Geology 27, 1023–1026.
Wintsch, R.P., Yi, K., 2002. Dissolution and replacement creep: a significant deformation mechanism in mid-crustal rocks. J. Struct. Geol. 24, 1179–1193.
Xing, L.B., Trail, D., Watson, E.B., 2013. Th and U partitioning between monazite and felsic melt. Chem. Geol. 358, 46–53.
Yakymchuk, C., Brown, M., 2014. Behaviour of zircon and monazite during crustal melting. Journal of the geological Society, London 171, 465–479.